Twisted Light Beam From a Gradient-Based Inverse-Designed Metasurface

Wei-Cheng Tsai, Po-Cheng Yang, An-Ru Yen, Yun-Chien Wu, and Yao-Wei Huang, *Member, IEEE*

***Abstract*—Optical vortex beams, characterized by helical wavefronts and orbital angular momentum (OAM), exhibit a phase singularity that forms a distinctive doughnut-shaped intensity profile. However, conventional observation methods often struggle to directly visualize their twisting behavior, limiting the ability to fully exploit spatial beam evolution in applications such as optical manipulation and three-dimensional structured light–matter interaction. In this work, we numerically and experimentally demonstrate a gradient-based inverse-design methodology to engineer metasurface capable of generating twisted light beams without predefined OAM or complex forward design processes. Our optimized metalens achieves precise triple-helical focusing, with focal spots consistently rotating by 40° clockwise across design focal planes and maintaining a stable radius of 2 μm. This approach offers significant potential for novel modes of optical tweezers and light-mater interaction, where controlled spatial rotation—distinct from traditional OAM-based beams—may enable new particle manipulation strategies, as well as for applications in imaging, lithography, and depth sensing.**

***Index Terms*—Gradient-based optimization, inverse design, metalens, metasurfaces, triple-helix focusing.**

I. Introduction

TWISTED light beams are most intuitively observed in vortex beams, which carry orbital angular momentum (OAM) [1], and can be generated through various methods including mode converters [2], spiral phase plates [3], fork gratings [4], *etc*. Based on polarization characteristics, vortex beams are classified into two distinct types. Scalar vortex beams exhibit uniform polarization distribution across their wavefront, while vector vortex beams demonstrate space-variant polarization in the plane transverse to the beam propagation direction [5]. Metasurfaces provide an alternative platform for vortex beam generation [6], implemented through various designs including q-plates [7], J-plates [8], [9], [10], and directionally asymmetric Janus metasurfaces [11]. These vortex beams carry orbital angular momentum states and exhibit circularly symmetric, donut-shaped intensity profiles. However, the twisting behavior of the Poynting vector is difficult to directly measure from the intensity profile alone and can only be determined through interferometric measurements of the beams' evolution. Therefore, some studies utilize beams with temporal correlations or combined time-frequency correlations to achieve control over beam twisting effects [12], [13], [14], [15]. Nevertheless, even with these time-frequency approaches, interferometric measurements are still required to observe the twisting behavior of the beam. Moreover, traditional OAM beams are particularly valuable in applications such as optical tweezers, where the intrinsic OAM enables rotational manipulation of trapped particles around the beam axis. However, such approaches primarily operate within fixed transverse planes and do not provide direct access to the beam's helical evolution along the propagation direction.

To observe beam-twisting effects without relying on a reference beam or interferometric measurements, researchers have developed various forward-design approaches. Specifically, these approaches utilize a rotation factor encoded in a heliconconical phase [16], implement orbital angular momentum encoded in Bessel functions [17], [18], or solve the metaharmonic boundary value problem of the Helmholtz wave equation [19]. By approximating the desired optical field, these methods generate twisted light beams as they propagate through space. Practically, twisted beams hold great promise for enhancing optical trapping by enabling complex three-dimensional particle assembly and offering new avenues for studying molecular dynamics in spatially structured environments [16], [17]. However, this approach becomes inefficient when optimizing multiple parameters simultaneously (such as helix focusing or multi-focusing), often requiring extensive computational resources while yielding limited performance. To overcome these limitations, inverse design approaches [20], including topology optimizations [21], [22], [23], machine learning [24], [25], evolutionary optimization [26], [27], genetic algorithms [28], and hybrid models of some of them [29], [30], may provide promising alternatives for implementing complex metasurface functionalities. In the context of twisted light beam, F. Yang et al. demonstrated a metalens design using an autonomous direct search algorithm for polarization-controlled double-helix beam twisting [31]. While effective for their specific application, this gradient-free approach may require more iterations to achieve convergence compared to gradient-based optimization methods. Additionally, Z. Li et al. utilized a gradient-based optimization method

Received 9 May 2025; revised 29 July 2025, 2 September 2025, and 18 September 2025; accepted 28 September 2025. Date of publication 1 October 2025; date of current version 2 December 2025. This work was supported in part by the National Science and Technology Council in Taiwan under Grant 113-2112-M-A49-025 and Grant 114-2112-M-A49-007, and in part by the Ministry of Education in Taiwan through Yushan Young Scholar Program. *(Corresponding author: Yao-Wei Huang.)*

The authors are with the Department of Photonics, College of Electrical and Computer Engineering, National Yang Ming Chiao Tung University, Hsinchu 300093, Taiwan (e-mail: jj510382.ee10@nycu.edu.tw; nycu300514098.c@nycu.edu.tw; anruyen.ee09@nycu.edu.tw; yunchien.ee11@nycu.edu.tw; ywh@nycu.edu.tw).

This article has supplementary material provided by the authors and color versions of one or more figures available at https://doi.org/10.1109/JLT.2025.3616368.

Digital Object Identifier 10.1109/JLT.2025.3616368

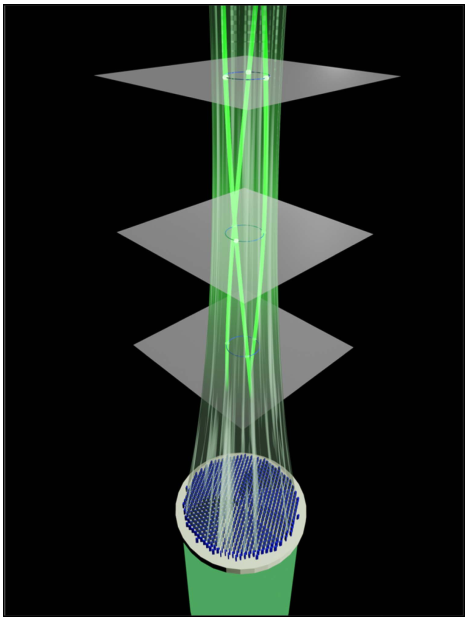

Fig. 1. Schematic diagram of a triple-helix focusing metalens designed using a gradient optimization method. The metasurface, with a radius of 10 μm, focuses incident light onto three planes located at $z = 31.8$ μm, 46.8 μm, and 61.8 μm in space. At each plane, the light converges to 3 focal points arranged in a circular pattern with a radius of 2 μm. As the distance from the metasurface increases, the positions of the focal points rotate, following the designed helical trajectory.

with regional parameter distributions to design achromatic metalenses with a diameter of up to 1 cm [32], but their approach did not address helix focusing or beam-twisting effects. Furthermore, polarization-insensitive optical functions can be readily achieved using polarization-insensitive nanopillars. Building upon these foundational frameworks, we extend the methodology to support multi-focal inverse design with polarization-insensitive nanopillars, enabling the controlled generation of twisted beams without relying on OAM.

In this paper, we demonstrate laser beam twisting using a metalens designed through multi-focusing via inverse design, as illustrated in Fig. 1. Our gradient optimization framework achieves triple-helix focusing across three focal planes, each contains 3 focal points positioned at a fixed radial distance of $r = 2$ μm from the optical axis and spaced 120° apart azimuthally. Between each pair of focal planes, the 3 focal spots maintain their designed radius of 2 μm and undergo a clockwise rotation of 40°. The 3 gray planes shown in Fig. 1 indicate the focal planes at z = 31.8 μm, 46.8 μm, 61.8 μm relative to the metalens, while the green beams illustrate the individual paths of the intensity profiles without OAM in the design. This gradient optimization framework enables efficient field computation and optimal structural distribution to achieve functional light beam twisting metasurfaces.

II. Optimization Framework and Metalens Design

Our framework integrates gradient-based optimization with rapid field calculations to enable complex optical functionalities. As shown in Fig. 2, the framework comprises three essential

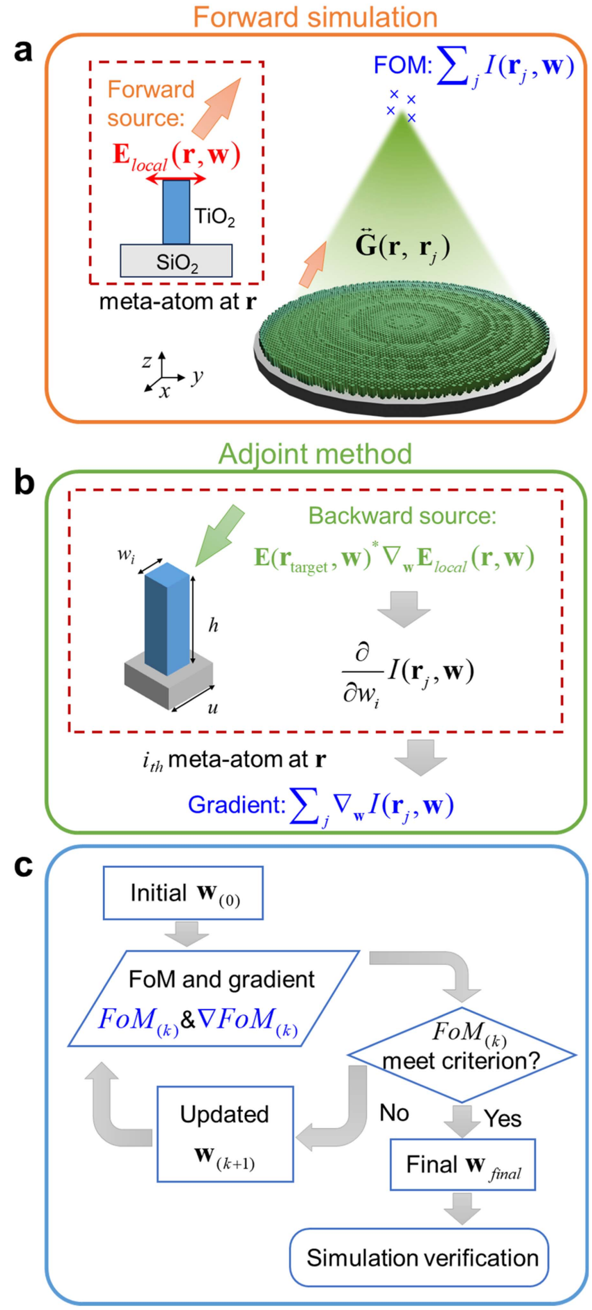

Fig. 2. Metalens designed using gradient optimization methods. (a) The intensity at the target position is rapidly calculated using the Hadamard product of the equivalent electric field and Green's function. (b) The adjoint method calculates the gradient of the metasurface structure with respect to the design parameters. (c) Flowchart of the inverse design process for metasurfaces. Utilizing a pre-established database of nanopillars, we initiate the optimization from a design region with randomly distributed widths.

components: forward simulation, adjoint calculation, and iterative optimization.

The forward simulation component, illustrated in Fig. 2(a), consists of two key elements: a local field computation from individual TiO_2 meta-atoms on a SiO_2 substrate, and a field propagation calculation using the Green's function. For each meta-atom positioned at location $\mathbf{r}$, the local electric field $\mathbf{E}_{\text{local}}(\mathbf{r}, \mathbf{w})$ is generated, where $\mathbf{w}$ represents the collective width parameters of the nanopillars. To find accelerate the computation of the total field intensity at a target position, we employ a Hadamard product operations between these local fields and the dyadic Green's function $\overleftrightarrow{\mathbf{G}}(\mathbf{r}, \mathbf{r}_{\text{target}})$ [32]:

$$I\left(\mathbf{r}_{\text{target}}, \mathbf{w}\right) = \left|\mathbf{E}\left(\mathbf{r}_{\text{target}}, \mathbf{w}\right)\right|^2 = \left|\int_{\Sigma} \mathbf{E}_{\text{local}}\left(\mathbf{r}, \mathbf{w}\right) \odot \overleftrightarrow{\mathbf{G}}\left(\mathbf{r}, \mathbf{r}_{\text{target}}\right) d\mathbf{r}\right|^2, \quad (1)$$

where $\overleftrightarrow{\mathbf{G}}(\mathbf{r}, \mathbf{r}_{\text{target}})$ describes the field propagation from the metasurface plane to the target focal positions $\mathbf{r}_{\text{target}}$. Notably, the Green's function $\overleftrightarrow{\mathbf{G}}(\mathbf{r}, \mathbf{r}_{\text{target}})$ needs to be computed only once during the optimization process, as it remains constant for fixed relative distances between the metasurface and focal points. This accelerates the optimization process. Considering multi-focusing functionality in our metasurface, the Figure of Merit (FOM), which quantifies the performance of our design, is computed by summing the intensities $I(\mathbf{r}_j, \mathbf{w})$ at target focal positions $\mathbf{r}_j$. Therefore, the total intensity produced at all focal points after electromagnetic wave propagation through the metalens, expressed as:

$$\text{FOM} = \sum_j I\left(\mathbf{r}_j, \mathbf{w}\right) = \sum_j \left|\int_{\Sigma} \mathbf{E}_{\text{local}}\left(\mathbf{r}, \mathbf{w}\right) \odot \overleftrightarrow{\mathbf{G}}\left(\mathbf{r}, \mathbf{r}_{\text{j}}\right) d\mathbf{r}\right|^2. \quad (2)$$

The FOM is calculated as the sum of intensities at all 9 focal points (3 focal points $\times$ 3 focal planes), as expressed in (2): $\text{FOM} = \sum_j I(\mathbf{r}_j, \mathbf{w})$. This formulation ensures that the optimization process considers all focal planes simultaneously during each iteration, enabling the metalens to achieve the desired helical focusing behavior while maintaining focal spot quality across all 3 focal planes.

To link the local electric field $\mathbf{E}_{\text{local}}(\mathbf{r}, \mathbf{w})$ with required meta-atoms, we employ a pre-computed local electric field database of meta-atoms using rigorous coupled-wave analysis (RCWA) based on the local periodic approximation [32]. Under the approximation, we assume the nanopillars are arranged in a periodic array where neighboring elements have minimal width variations, allowing us to treat the electromagnetic wave interaction as if passing through a periodic interface of identical pillars. This approximation enables efficient RCWA calculations of the field at the metasurface interface, creating a comprehensive database that relates nanopillar widths to their corresponding amplitude, phase, and transmission characteristics. As illustrated inset of Fig. 2(a), TiO_2 square nanopillars on SiO_2 substrate are designed as meta-atoms of metasurface to generate each local electric field. The geometry parameters are shown in the inset of Fig. 2(b), where w_i represents the width of individual meta-atoms, h denotes the nanopillar height, and u indicates the period of the meta-atom array. The square geometry of these nanopillars was specifically chosen for its polarization-independent response, as it maintains consistent efficiency across different incident light polarization states.

To efficiently compute the gradient for optimization, we employ the adjoint method, as shown in Fig. 2(b). Following the derivation of intensity at a target position, the gradient can be expressed as:

$$\nabla_{\mathbf{w}} I\left(\mathbf{r}_{\text{target}}, \mathbf{w}\right) = 2\Re\left[\int_{\Sigma} \mathbf{E}(\mathbf{r}_{\text{target}}, \mathbf{w})^* \nabla_{\mathbf{w}} \mathbf{E}_{\text{local}}\left(\mathbf{r}, \mathbf{w}\right) \odot \overleftrightarrow{\mathbf{G}}\left(\mathbf{r}, \mathbf{r}_{\text{target}}\right) d\mathbf{r}\right], \quad (3)$$

where $\Re$ represents the real part of a complex value, $\mathbf{E}(\mathbf{r}_{\text{target}}, \mathbf{w})^*$ is the conjugate of field at the target position, and $\nabla_{\mathbf{w}} \mathbf{E}_{\text{local}}(\mathbf{r}, \mathbf{w})$ is the gradient of the local field at the meta-atoms. Therefore, considering multipole target focal positions, the gradient of FOM is then the sum of all gradients at all focal points, expressed as:

$$\nabla_{\mathbf{w}}\text{FOM} = \sum_j \nabla_{\mathbf{w}} I\left(\mathbf{r}_j, \mathbf{w}\right) = \sum_j 2\Re\left[\int_{\Sigma} \mathbf{E}(\mathbf{r}_j, \mathbf{w})^* \nabla_{\mathbf{w}} \mathbf{E}_{\text{local}}\left(\mathbf{r}, \mathbf{w}\right) \odot \overleftrightarrow{\mathbf{G}}\left(\mathbf{r}, \mathbf{r}_j\right) d\mathbf{r}\right]. \quad (4)$$

The total gradient is expressed as the sum of intensity gradients at each focal point. The calculation employs an equivalent backward source $\mathbf{E}(\mathbf{r}_j, \mathbf{w})^* \nabla_{\mathbf{w}} \mathbf{E}_{\text{local}}(\mathbf{r}, \mathbf{w})$, providing an efficient method for gradient computation across the entire metasurface structure. In this formulation, $\nabla_{\mathbf{w}} \mathbf{E}_{\text{local}}(\mathbf{r}, \mathbf{w})$ denotes the gradient of the local electromagnetic field with respect to the width parameter w at each meta-atom position r on the metasurface plane. This local field gradient is efficiently retrieved from a pre-computed database, significantly reducing computational complexity by eliminating the need for repetitive RCWA calculations. The gradient term $\nabla_{\mathbf{w}} I(\boldsymbol{r}_j, \mathbf{w})$ provides crucial information about the sensitivity of the *j*th focal intensity to width variations of individual meta-atoms. When evaluated across the entire metasurface, this generates a comprehensive gradient distribution $\sum_j \nabla_{\boldsymbol{w}} I(\boldsymbol{r}_j)$ for the subsequent optimization iterations.

The key advantage of this approach lies in its computational efficiency. A traditional brute-force approach would require $N+1$ simulations for N design parameters—one forward simulation and N individual perturbations corresponding to each nanopillar parameter. In contrast, the adjoint method achieves complete gradient information using only a few simulations: one forward simulation to compute the focal field and one adjoint simulation for each equivalent source [32]. In our implementation, we employ a total of 9 adjoint sources, each positioned at a designated focal point. This significant reduction in computational cost makes it practical to optimize large-scale metasurfaces containing thousands of individual nanopillars. Gradient information, efficiently obtained everywhere at once through the adjoint simulation, is fed into the optimization framework. This enables systematic updates of the nanopillar width distribution through successive optimization iterations.

The practical implementation of the optimization framework follows the process illustrated in Fig. 2(c) to establish specific optimization parameters. The optimization process is initialized with a pre-established database of nanopillars, where the design region begins with randomly distributed widths. This systematic approach encompasses several key parameters: the upper and lower bounds of optimization variables, gradient definitions of the objective function, maximum iteration count, and optimization method configuration with appropriate termination conditions. The iterative optimization loop consists of two main components: a forward simulator for field calculations and the adjoint method for gradient computation. During each iteration, the framework calculates both the FOM and its gradient to guide the design evolution. These calculations enable systematic updates of the nanopillar width distribution. The iteration process continues until meeting specified termination criteria, at which point the final component undergoes simulation verification to evaluate its efficiency.

III. Triple-Helix Focusing

To achieve light beam twisting functionality, the metasurface design was developed to create rotating focal points, termed as triple-helix focusing. The meta-atom library consists of square-shaped TiO_2 nanopillars with a height (h) of 600 nm, arranged in a square lattice with a periodicity (u) of 250 nm. The lateral dimensions (w_i) of the square nanopillars range from 80 nm to 200 nm, allowing full 2π phase coverage for effective wavefront control. The triple-helix focusing metalens has a diameter of 20 μm, consisting of 5024 meta-atoms. The metasurface generates three distinct focal planes located at $z_1 = 31.8$ μm, $z_2 = 46.8$ μm, and $z_3 = 61.8$ μm along the optical axis. Within each focal plane, 3 focal points are arranged in a circular pattern with a radius of 2 μm. As the beam propagates, the entire triangular arrangement undergoes a clockwise rotation of 40° between consecutive planes, creating a helical focusing trajectory. The 40° angular offset was selected based on geometric considerations to ensure systematic progression and sufficient angular separation for experimental resolution. With 3 focal points per plane spaced 120° apart, a 40° offset corresponds to a one-third rotation of the triangular pattern between planes—resulting in a symmetric, helical-like target configuration that is both visually distinct and experimentally measurable.

Fig. 3 illustrates changes in FOM and structural parameters as the optimization process of our metasurface design. In Fig. 3(a), the plot tracks the FOM evolution, where the relationship between iteration number and FOM is shown with key optimization points marked by green stars. The optimization demonstrates steady improvement from an initial low FOM value, ultimately reaching approximately 236000 after 426 iterations. These optimization points represent significant structural modifications in the metasurface design, leading to enhanced electromagnetic wave control. The evolution of structural parameters of the metalens is presented in Fig. 3(b), where each subfigure corresponds to a specific optimization stage. Using a color scale to represent the nanopillar width distribution, the sequence captures three critical stages: the initial structure (iteration 1) with relatively low FOM, an intermediate state (iteration 55) showing substantial structural refinements, and the final optimized configuration

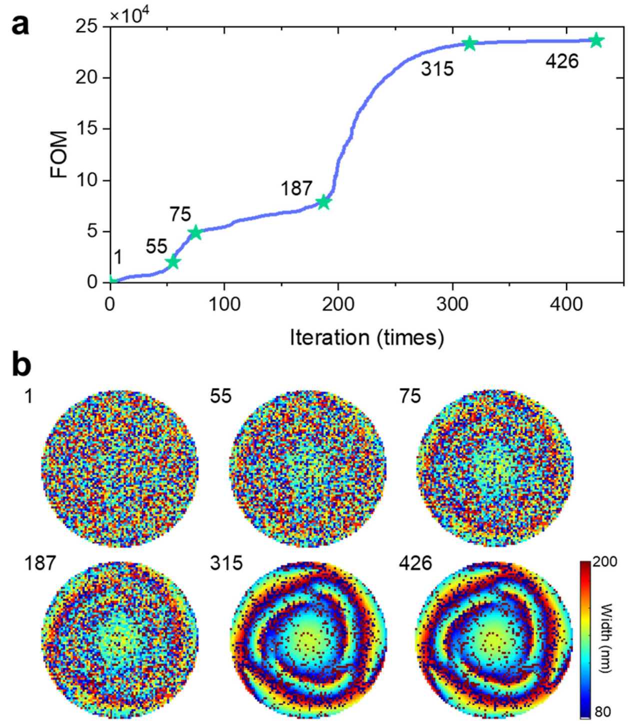

Fig. 3. Iteration process. (a) Iteration process of metalens with enhancement on FOM. (b) Structural evolution of triple-helix focusing metalens.

(iteration 426) achieving the highest FOM value. The optimization process requires approximately 2 hours of computational time. Details regarding the computer specifications and software used are provided in Supplementary Material S1. The final width distribution of the designed triple-helix focusing metalens exhibits a characteristic three-petal flower pattern. This distinctive phase configuration drives the focal points to rotate clockwise across the focal planes, successfully achieving the desired light beam twisting functionality that difficult to theoretically achieve with forward design.

Throughout this optimization process, the systematic refinement of nanopillar width distribution enables precise control over both phase and amplitude of the transmitted light. The gradient-based optimization method guides this evolution from initial to optimized design, achieving complex optical functionalities. The direct correlation between FOM improvements and structural modifications demonstrates the effectiveness of our optimization approach in refining the metalens design.

The fabrication of our triple-helix focusing metalens involves a series of precisely controlled processes. These include electron beam lithography (EBL), atomic layer deposition (ALD) of TiO_2, high-density plasma reactive ion etching (HDP-RIE), and e-beam resist removal. The fabrication methodology follows established protocols described in the literature [11], [33], with specific modifications detailed in Supplementary Material S2. This optimized process enables the creation of nanopillars with superior vertical sidewalls and high aspect ratios compared to conventional top-down fabrication methods. To ensure precise optical characterization, we fabricate a chromium (Cr) aperture using ultraviolet lithography followed by Cr deposition and

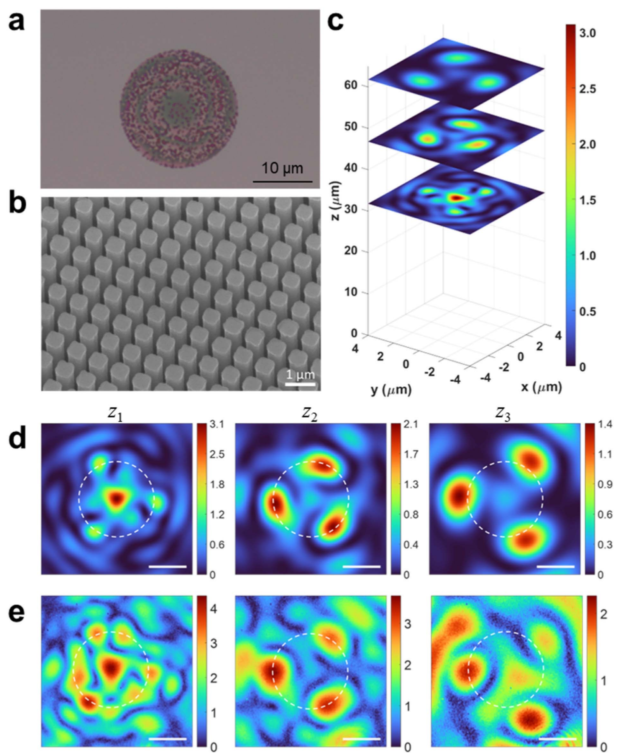

Fig. 4. The demonstration of triple helix focusing. (a) Optical microscope image of the fabricated sample. (b) Scanning electron microscope (SEM) image revealing the nanopillar of the sample. (c) Simulated intensity profile along the optical axis at the designed planes. The simulation verification demonstrates the spatial evolution of intensity as the beam propagates through the triple helix focusing metalens. Color bar: Intensity (a.u.). (d) Simulated intensity distributions at the designed planes White d ashed circles represent a radius of 2 μm). Scalebar: 2 µm. Color bar: Intensity (a.u.). (e) Experimentally measured intensity distributions at the designed planes. Scalebar: 2 µm. Color bar: Intensity (a.u.).

lift-off processes, which effectively confines light transmission to the metalens area. Fig. 4(a) shows an optical microscope image of the metasurface, revealing a complex arrangement of nanopillars that results from our inverse design optimization. The width-dependent optical response of individual nanopillars manifests as varying reflective colors in the visible regime, creating a pattern that corresponds to the width distribution presented in Fig. 3(b)(iteration 426), displaying the characteristic trilateral symmetry of the designed metasurface. Scanning electron microscopy (SEM) analysis of the fabricated structure (Fig. 4(b)) confirms the high quality of our TiO_2 nanopillars, exhibiting exceptional vertical sidewalls and smooth surfaces, validating the precision of our fabrication methodology.

We achieve simulated characterization of our design in advance for comparison with experimental demonstration. In simulation verification, our triple-helix focusing metalens design demonstrates well-controlled light manipulation capabilities. Fig. 4(c) illustrates the simulated three-dimensional intensity distribution, with focal planes positioned at z_1, z_2, and z_3, each separated by 15 μm intervals. The 3 planes share a color bar, revealing that the focal spots in the 2nd and 3rd planes exhibit notably lower intensities compared to the first plane. Additionally, the intensity distributions at each focal plane are presented in Fig. 4(d) with individual color bars, allowing for clearer visualization of the focal spot patterns within each plane regardless of their absolute intensity differences. At each focal plane, focal spots successfully exhibit a district clockwise rotation of 40° between precise planes with a radius of approximately 2 μm (white dashed line in Fig. 4(d)). In the optimized design, while the 1st plane shows stronger central intensity without distinct focusing at the designed locations, the 2nd and 3rd planes exhibit well-defined focal spots at the intended positions. Notably, the focal points demonstrate a non-uniform rotation along the propagation direction, as shown in the Supplementary Video. Specifically, continuous rotation is observed between the 2nd and 3rd focal planes, but not between the 1st and 2nd. This behavior reflects inherent electromagnetic constraints and suggests that helical focusing is subject to propagation-dependent limitations. The interruption of rotation between the 1st and 2nd planes may result from destructive interference, whereas the continuous rotation between the 2nd and 3rd planes likely arises from constructive interference. Introducing non-uniform rotation angles between focal planes or adjusting their axial positions may help sustain constructive interference throughout the beam's propagation path. The simulated intensity distributions shown in Fig. 4(d) reveal precise control over both the spatial positioning of focal spots and their rotational evolution, demonstrating the effectiveness of our inverse design approach in achieving complex optical functionalities.

We utilized a hand-made optical setup to measure the intensity profile, detailed in Supplementary Material S3. The experimental characterization of the fabricated device, presented in Fig. 4(e) and Supplementary Video, shows the measured intensity distributions at the corresponding focal planes. These experimental results show excellent agreement with our simulated predictions (Fig. 4(d)), particularly in terms of the overall rotational behavior. All 3 planes were designed with identical radii of 2 μm (labeled with white dashed circles) without presupposing convergence or divergence behavior. However, our simulation and experimental results demonstrate progressive divergence from the 1st to 3rd focal planes, indicating that the optimized metalens exhibits a relatively short focal length. To address this limitation, one could introduce progressive convergence—*e.g.*, decreasing the focal spot radius from the 1st to 3rd focal planes. Additionally, while the simulated focal spots exhibit significantly higher intensities than the unwanted diffraction spots, the experimental measurements reveal that some designed focal spots show reduced intensity relative to surrounding spurious spots. We attribute this discrepancy to fabrication imperfections that alter the meta-atom profiles responsible for specific focal points. Such deviations can reduce the focusing efficiency of certain nanopillars, leading to partial redirection of energy away from the intended focal spots and toward unwanted diffraction regions. This results in the observed intensity redistribution.

To further characterize the beam properties and validate our design methodology, we performed comprehensive modal analysis of the generated twisted beam. Although our initial design did not explicitly encode OAM components, the optimized twisted beam exhibits OAM content that naturally arises from the inverse design process. We conducted Laguerre-Gaussian

(LG) modal decomposition analysis on the simulated electric field distribution using established techniques [34], [35]. Our analysis reveals that the generated twisted beam is primarily composed of three dominant LG modes: $LG_{0,2}$ (24.4%), $LG_{0,0}$ (18.0%), and $LG_{-3,1}$ (17.3%), together accounting for 59.78% of the total beam energy. The presence of the $LG_{-3,1}$ mode, with a topological charge of -3, confirms that OAM components emerged intrinsically from the optimization, even though they were not explicitly included in the design objectives. Detailed LG mode decomposition results and the associated mathematical framework are provided in Supplementary Material S4.

To benchmark the performance of our inverse design approach, we compared its numerical focusing efficiency against a forward design baseline. We constructed an ideal forward-designed beam by linearly superposing the 3 dominant LG modes ($LG_{0,2}$, $LG_{0,0}$, and $LG_{-3,1}$) with their respective weight coefficients. The forward design approach achieved an absolute focusing efficiency of 6.82%, whereas our inverse design methodology demonstrated a significantly higher absolute efficiency of 35.62%. This substantial improvement—more than a 5-fold increase—highlights the superior performance of our gradient-based optimization framework compared to conventional forward design approaches based on modal superposition. Detailed information can be found in Supplementary Material S5.

IV. Conclusion

This study presents an inverse design framework for metalens optimization, incorporating a computationally efficient solver that utilizes Green's function for rapid calculation of target electromagnetic fields and gradients. Through this framework, we have successfully demonstrated the design and implementation of a triple-helical focusing metalens with unique optical functionalities. The proposed metalens achieves controlled light focusing at three distinct points along the optical axis, seamlessly transforming discrete focal points into a continuous helical focal trajectory.

Our design methodology offers several significant advantages. First, the integration of Green's function with gradient-based optimization significantly reduces computational complexity while maintaining high accuracy in the design process. Second, the inverse design framework provides flexibility in implementing complex optical functionalities, enabling the creation of novel metalens designs that were previously challenging to achieve in forward design.

The experimental validation of our design was accomplished through ALD technology for the TiO_2 nanopillars, demonstrating excellent fabrication quality. SEM characterization reveals well-formed nanopillars featuring vertical sidewalls and refined surface characteristics, crucial for optimal optical performance. The experimental measurements show remarkable agreement with simulated results, validating both our design methodology and fabrication approach.

While the system demonstrates promising results, there are opportunities for future improvements. Further optimization of the fabrication process could enhance the structural uniformity of nanopillars, potentially leading to even better optical performance. Additionally, extending this design framework to other complex optical functionalities could broaden its applications.

In conclusion, we present a comprehensive framework for the design and fabrication of inverse-designed metalenses, combining theoretical optimization with experimental implementation. The successful demonstration of controlled triple-helical focusing not only advances the capabilities of structured light generation but also enables new rotational degrees of freedom in beam shaping that are difficult to achieve using conventional OAM-based. This expanded design space may facilitate novel forms of optical trapping [16], [17] and light–matter interaction [36], [37], alongside practical applications in depth sensing [31], wavefront-based imaging [38], and high-resolution microscopy [39].

IV. Supplementary Information

Supplementary Video shows the rotation of focal spots as light propagates through the triple-helix focusing metalens, which was captured using an automated translation stage for precise z-axis control (MP4). Supplementary Material S1-S5 contents computation cost of optimization process, fabrication process, experimental setup for intensity measurement, Laguerre-Gaussian mode decomposition, and efficiency comparison between inverse and forward design (PDF).

Acknowledgment

The authors acknowledge that part of the fabrication and characterization was carried out using instruments and facilities at the Nano Facility Center (NFC) and the Center for Nano Science and Technology (CNST) of National Yang Ming Chiao Tung University, and at the Taiwan Semiconductor Research Institute (TSRI). The authors also acknowledge Ms. Yu-Chen Yeh for drawing the schematic diagram of the triple-helix focusing metalens.

References

[1] Y. Shen et al., "Optical vortices 30 years on: OAM manipulation from topological charge to multiple singularities," *Light: Sci. Appl.*, vol. 8, no. 1, Oct. 2019, Art. no. 90, doi: 10.1038/s41377-019-0194-2.

[2] L. Allen, M. W. Beijersbergen, R. J. C. Spreeuw, and J. P. Woerdman, "Orbital angular momentum of light and the transformation of Laguerre-Gaussian laser modes," *Phys. Rev. A*, vol. 45, no. 11, pp. 8185–8189, Jun. 1992, doi: 10.1103/PhysRevA.45.8185.

[3] M. W. Beijersbergen, R. P. C. Coerwinkel, M. Kristensen, and J. P. Woerdman, "Helical-wavefront laser beams produced with a spiral phaseplate," *Opt. Commun.*, vol. 112, no. 5, pp. 321–327, Dec. 1994, doi: 10.1016/0030-4018(94)90638-6.

[4] V. Y. Bazhenov, M. V. Vasnetsov, and M. S. Soskin, "Laser beams with screw dislocations in their wavefronts," *JETP Lett.*, vol. 52, no. 52, pp. 429–431, 1990.

[5] V. Aita, M. Shevchenko, F. J. Rodríguez-Fortuño, and A. V. Zayats, "Propagation of focused scalar and vector vortex beams in anisotropic media: A semianalytical approach," *Phys. Rev. B*, vol. 109, no. 12, Mar. 2024, Art. no. 125433, doi: 10.1103/PhysRevB.109.125433.

[6] M. L. Brongersma et al., "The second optical metasurface revolution: Moving from science to technology," *Nature Rev. Elect. Eng.*, vol. 2, no. 2, pp. 125–143, Feb. 2025, doi: 10.1038/s44287-024-00136-4.

[7] R. C. Devlin et al., "Spin-to-orbital angular momentum conversion in dielectric metasurfaces," *Opt. Exp.*, vol. 25, no. 1, pp. 377–393, Jan. 2017, doi: 10.1364/OE.25.000377.

[8] R. C. Devlin, A. Ambrosio, N. A. Rubin, J. P. B. Mueller, and F. Capasso, "Arbitrary spin-to–orbital angular momentum conversion of light," *Science*, vol. 358, no. 6365, pp. 896–901, Nov. 2017, doi: 10.1126/science.aao5392.

[9] Y.-W. Huang et al., "Versatile total angular momentum generation using cascaded J-plates," *Opt. Exp.*, vol. 27, no. 5, pp. 7469–7484, Mar. 2019, doi: 10.1364/OE.27.007469.

[10] H. Sroor et al., "High-purity orbital angular momentum states from a visible metasurface laser," *Nature Photon.*, vol. 14, no. 8, pp. 498–503, Aug. 2020, doi: 10.1038/s41566-020-0623-z.

[11] C.-Y. Lin, J.-H. Huang, H.-T. Su, S.-M. Chang, Y.-C. Wu, and Y.-W. Huang, "Directionally asymmetric in orbital angular momentum generation using single-layer dielectric Janus metasurfaces," *Adv. Opt. Mater.*, vol. 12, no. 31, 2024, Art. no. 2401335, doi: 10.1002/adom.202401335.

[12] M. Piccardo et al., "Broadband control of topological–spectral correlations in space–time beams," *Nature Photon.*, vol. 17, no. 9, pp. 822–828, Sep. 2023, doi: 10.1038/s41566-023-01223-y.

[13] B. Chen et al., "Integrated optical vortex microcomb," *Nature Photon.*, vol. 18, no. 6, pp. 625–631, Jun. 2024, doi: 10.1038/s41566-024-01415-0.

[14] J. Zhang, P. Li, R. C. C. Cheung, A. M. H. Wong, and J. Li, "Generation of time-varying orbital angular momentum beams with space-time-coding digital metasurface," *Proc. SPIE*, vol. 5, no. 3, Apr. 2023, Art. no. 036001, doi: 10.1117/1.AP.5.3.036001.

[15] Y. Shen et al., "Roadmap on spatiotemporal light fields," *J. Opt.*, vol. 25, no. 9, Aug. 2023, Art. no. 093001, doi: 10.1088/2040-8986/ace4dc.

[16] J. Hu, W. Wei, Z. Sun, X. Li, and Y. Qian, "Customizing twisted structured light beams," *Opt. Laser Technol.*, vol. 181, Feb. 2025, Art. no. 111708, doi: 10.1016/j.optlastec.2024.111708.

[17] A. H. Dorrah, M. Zamboni-Rached, and M. Mojahedi, "Controlling the topological charge of twisted light beams with propagation," *Phys. Rev. A*, vol. 93, no. 6, Jun. 2016, Art. no. 063864, doi: 10.1103/PhysRevA.93.063864.

[18] A. H. Dorrah, N. A. Rubin, A. Zaidi, M. Tamagnone, and F. Capasso, "Metasurface optics for on-demand polarization transformations along the optical path," *Nature Photon.*, vol. 15, no. 4, pp. 287–296, Apr. 2021, doi: 10.1038/s41566-020-00750-2.

[19] Y. Aborahama, A. H. Dorrah, and M. Mojahedi, "Designing the phase and amplitude of scalar optical fields in three dimensions," *Opt. Exp.*, vol. 28, no. 17, pp. 24721–24730, Aug. 2020, doi: 10.1364/OE.397119.

[20] Z. Li, R. Pestourie, Z. Lin, S. G. Johnson, and F. Capasso, "Empowering metasurfaces with inverse design: Principles and applications," *ACS Photon.*, vol. 9, no. 7, pp. 2178–2192, Jul. 2022, doi: 10.1021/acsphotonics.1c01850.

[21] H.-T. Su et al., "Topology optimization enables high-Q metasurface for color selectivity," *Nano Lett.*, vol. 24, no. 33, pp. 10055–10061, Aug. 2024, doi: 10.1021/acs.nanolett.4c01858.

[22] D. Sell, J. Yang, S. Doshay, R. Yang, and J. A. Fan, "Large-angle, multifunctional metagratings based on freeform multimode geometries," *Nano Lett.*, vol. 17, no. 6, pp. 3752–3757, Jun. 2017, doi: 10.1021/acs.nanolett.7b01082.

[23] Y.-T. Liu, Y.-C. Wu, C.-Y. Lin, H.-T. Su, Y.-Q. Zhou, and Y.-W. Huang, "Topology optimization enables freeform matrix Fourier optics," *Adv. Opt. Mater.*, vol. 13, no. 24, Aug. 2025, Art. no. 2500872, doi: 10.1002/adom.202500872.

[24] W. Ma, Z. Liu, Z. A. Kudyshev, A. Boltasseva, W. Cai, and Y. Liu, "Deep learning for the design of photonic structures," *Nature Photon.*, vol. 15, no. 2, pp. 77–90, Feb. 2021, doi: 10.1038/s41566-020-0685-y.

[25] C.-H. Lin, S.-H. Huang, T.-H. Lin, and P. C. Wu, "Metasurface-empowered snapshot hyperspectral imaging with convex/deep (CODE) small-data learning theory," *Nature Commun.*, vol. 14, no. 1, Nov. 2023, Art. no. 6979, doi: 10.1038/s41467-023-42381-5.

[26] M. Y. Shalaginov et al., "Design for quality: Reconfigurable flat optics based on active metasurfaces," *Nanophotonics*, vol. 9, no. 11, pp. 3505–3534, Sep. 2020, doi: 10.1515/nanoph-2020-0033.

[27] D. Z. Zhu, E. B. Whiting, S. D. Campbell, D. B. Burckel, and D. H. Werner, "Optimal high efficiency 3D plasmonic metasurface elements revealed by lazy ants," *ACS Photon.*, vol. 6, no. 11, pp. 2741–2748, Nov. 2019, doi: 10.1021/acsphotonics.9b00717.

[28] W.-L. Hsu et al., "Simplest but efficient design of a color router optimized by genetic algorithms," *ACS Photon.*, vol. 12, no. 3, pp. 1402–1408, Mar. 2025, doi: 10.1021/acsphotonics.4c01905.

[29] J. Jiang, D. Sell, S. Hoyer, J. Hickey, J. Yang, and J. A. Fan, "Free-form diffractive metagrating design based on generative adversarial networks," *ACS Nano*, vol. 13, no. 8, pp. 8872–8878, Aug. 2019, doi: 10.1021/acsnano.9b02371.

[30] J. Jiang and J. A. Fan, "Global optimization of dielectric metasurfaces using a physics-driven neural network," *Nano Lett.*, vol. 19, no. 8, pp. 5366–5372, Aug. 2019, doi: 10.1021/acs.nanolett.9b01857.

[31] F. Yang, H.-I. Lin, P. Chen, J. Hu, and T. Gu, "Monocular depth sensing using metalens," *Nanophotonics*, vol. 12, no. 14, pp. 2987–2996, Jul. 2023, doi: 10.1515/nanoph-2023-0088.

[32] Z. Li, R. Pestourie, J.-S. Park, Y.-W. Huang, S. G. Johnson, and F. Capasso, "Inverse design enables large-scale high-performance meta-optics reshaping virtual reality," *Nature Commun.*, vol. 13, no. 1, May 2022, Art. no. 2409, doi: 10.1038/s41467-022-29973-3.

[33] R. C. Devlin, M. Khorasaninejad, W. T. Chen, J. Oh, and F. Capasso, "Broadband high-efficiency dielectric metasurfaces for the visible spectrum," *Proc. Nat. Acad. Sci.*, vol. 113, no. 38, pp. 10473–10478, Sep. 2016, doi: 10.1073/pnas.1611740113.

[34] C. Schulze, A. Dudley, D. Flamm, M. Duparré, and A. Forbes, "Measurement of the orbital angular momentum density of light by modal decomposition," *New J. Phys.*, vol. 15, no. 7, Jul. 2013, Art. no. 073025, doi: 10.1088/1367-2630/15/7/073025.

[35] I. Nape et al., "Enhancing the modal purity of orbital angular momentum photons," *APL Photon.*, vol. 5, no. 7, Jul. 2020, Art. no. 070802, doi: 10.1063/5.0005597.

[36] G. Ruffato, "Non-destructive OAM measurement via light–matter interaction," *Light: Sci. Appl.*, vol. 11, no. 1, Mar. 2022, Art. no. 55, doi: 10.1038/s41377-022-00749-0.

[37] V. Grillo et al., "Observation of nanoscale magnetic fields using twisted electron beams," *Nature Commun.*, vol. 8, no. 1, Sep. 2017, Art. no. 689, doi: 10.1038/s41467-017-00829-5.

[38] F. Sanson et al., "Highly multimodal structure of high topological charge extreme ultraviolet vortex beams," *Opt. Lett.*, vol. 45, no. 17, pp. 4790–4793, Sep. 2020, doi: 10.1364/OL.397206.

[39] M. Pancaldi et al., "High-resolution ptychographic imaging at a seeded free-electron laser source using OAM beams," *Optica*, vol. 11, no. 3, pp. 403–411, Mar. 2024, doi: 10.1364/OPTICA.509745.